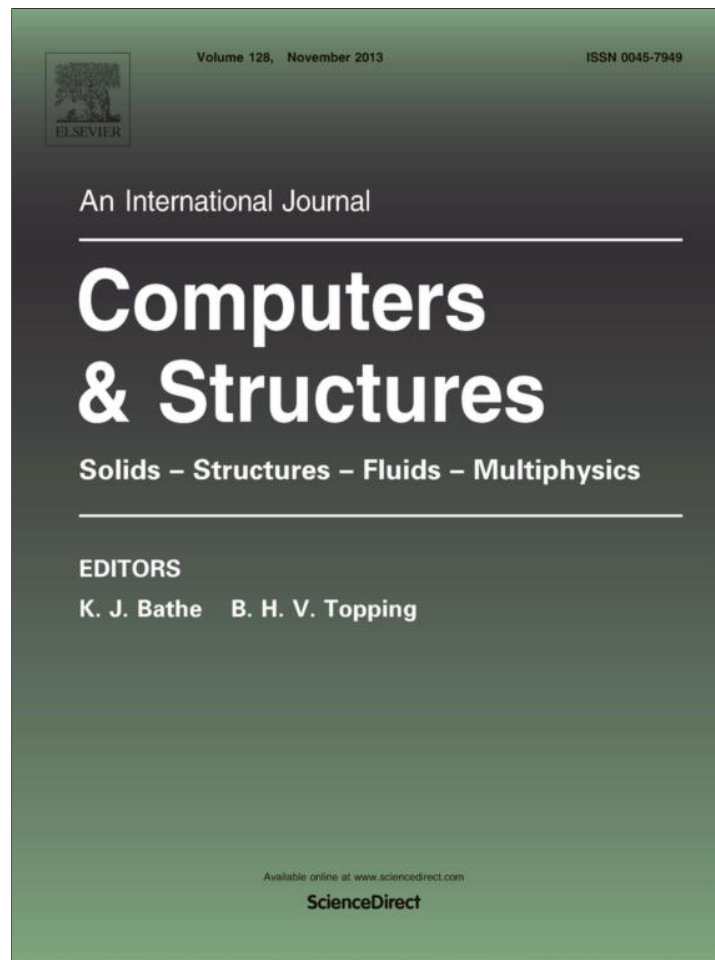


Provided for non-commercial research and education use.
Not for reproduction, distribution or commercial use.



This article appeared in a journal published by Elsevier. The attached copy is furnished to the author for internal non-commercial research and education use, including for instruction at the authors institution and sharing with colleagues.

Other uses, including reproduction and distribution, or selling or licensing copies, or posting to personal, institutional or third party websites are prohibited.

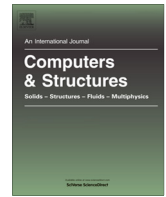
In most cases authors are permitted to post their version of the article (e.g. in Word or Tex form) to their personal website or institutional repository. Authors requiring further information regarding Elsevier's archiving and manuscript policies are encouraged to visit:

<http://www.elsevier.com/authorsrights>



Contents lists available at ScienceDirect

Computers and Structures

journal homepage: www.elsevier.com/locate/compstruc

A two-scale micromechanical model for aluminium foam based on results from nanoindentation



Jiří Němeček*, Vlastimil Králík, Jaroslav Vondřejc

Czech Technical University in Prague, Faculty of Civil Engineering, Department of Mechanics, Thákurova 7, 16629 Prague 6, Czech Republic

ARTICLE INFO

Article history:

Received 14 February 2013

Accepted 25 July 2013

Available online 13 September 2013

Keywords:

Aluminium foam

Multi-scale model

Nanoindentation

Statistical deconvolution

Elastic properties

Image analysis

ABSTRACT

The main aim of this paper is to develop and verify simple but effective model for elastic properties of a porous aluminium foam system and to compare results received from experimental micromechanics with solutions given by analytical or more advanced numerical methods. The material is characterized by a closed pore system with very thin but microscopically inhomogeneous pore walls (~ 0.1 μm) and large air pores (~ 2.9 μm). Therefore, two material levels can be distinguished. The lower level of the proposed model contains inhomogeneous solid matter of the foam cell walls produced from an aluminium melted with admixtures. Elastic parameters as well as volume fractions of microstructural material phases at this level are assessed with nanoindentation and effective properties computed via analytical and numerical homogenization schemes. The effective Young's modulus of the cell walls was found close to 70 GPa irrespective to the used homogenization procedure.

The higher model scale contains homogenized cell walls and a significant volume fraction of air voids (91.4%). Since analytical schemes fail to predict effective properties of this highly porous structure, numerical homogenization based on a simple two dimensional finite element model is utilized. The model geometry is based on foam optical images from which an equivalent beam structure is produced using Voronoi tessellation. Effective foam Young's modulus was found to be 1.36–1.38 GPa which is in relation with ~ 1.45 GPa obtained from uniaxial compression experiments.

© 2013 Elsevier Ltd. All rights reserved.

1. Introduction

Metal foams and especially lightweight aluminium foams belong to the group of up-to-date engineering materials with high potential to many applications. Metal foam is a highly porous hierarchical material with a cellular microstructure. Macroscopically, it can be characterized by attractive mechanical and physical properties such as high stiffness and strength in conjunction with very low weight, excellent impact energy absorption, high damping capacity and good sound absorption capability. The usual source material for the production of metal foams are aluminium and aluminium alloys because of low specific density (~ 2700 kg/m^3), low melting point (~ 660 $^\circ\text{C}$), non-flammability, possibility of recycling and excellent corrosion resistance. The metal foams are used in applications ranging from automotive and aerospace industries (e.g. bumpers, car body sills, motorcycle helmets) to building industry (e.g. sound proofing panels). Our aim has been to characterize and to model a commercially available foam Alporas produced by Shinko Wire Company, Ltd. This paper, that is devoted

to the micromechanical characterization of this material, is an updated and revised version of the conference paper [1].

Alporas [2,3] is characterized with a hierarchical system of pores containing different cell morphologies (in shape and size) depending on the foam density and inhomogeneous material properties of the cell walls [2,4]. A typical cross section of the foam can be seen in Fig. 1 where large pores (having typically 1–13 mm in diameter) are shown with detailed view on thin walls (~ 100 μm thick).

It follows from its hierarchical microstructure that the mechanical properties of metal foams are governed by two major factors:

- (i) cell morphology (shape, size, and distribution of cells) and
- (ii) material properties of the cell walls [4].

Traditionally, mechanical properties of metal foams are obtained using conventional macroscopic testing techniques on large samples that can give overall (effective) properties, e.g. [5–10]. However, conventional measurements face significant obstacles in the form of very small dimensions of cell walls, low local bearing capacity, local yielding, and bending of the cell walls. These problems can be overcome using micromechanical experimental methods in which the load–displacement curve is obtained in the

* Corresponding author. Tel.: +420 224354309.

E-mail address: jiri.nemecek@fsv.cvut.cz (J. Němeček).

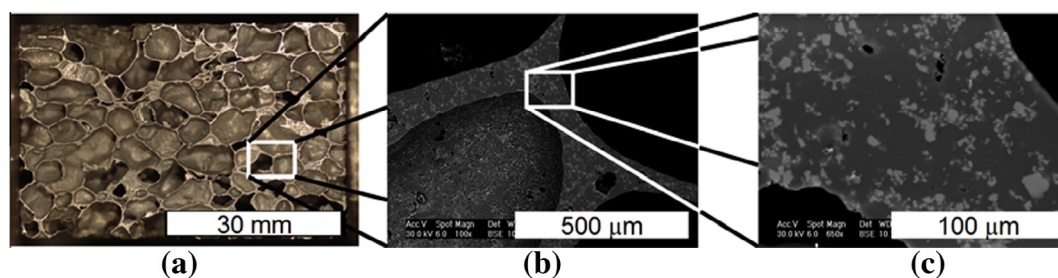


Fig. 1. (a) Overall view on a foam structure (further denoted as Level II); (b) SEM image of a cell wall; (c) detailed SEM image of a cell wall (denoted as Level I) showing Al-rich (dark grey) and Ca/Ti-rich areas (light zones).

sub-micrometer range. A few attempts have been carried out in the past, e.g. [4,7].

The paper develops a bottom-up approach for modeling the elastic properties of metal foam starting from lower level at which microscopic measurements, nanoindentation, and statistical deconvolution for the phase separation [11–13] are utilized. Compared to traditional macroscopic techniques, nanoindentation can distinguish between individual inhomogeneous microstructural entities. The effective cell wall properties have been obtained through analytical and numerical up-scaling techniques [14].

Finally, simple 2-D finite element model for the upper composite scale has been proposed and results validated against full-scale experiments.

2. Experimental part

2.1. Materials and sample preparation

Commercial aluminium foam Alporas® (Shinko Wire Company, Ltd) was used in this study. The manufacturing process of the Alporas is a batch casting process [3] in which 1.5 wt.% of calcium is added to the aluminium molten at 680 °C. Calcium serves as a thickening agent which increases viscosity and stabilizes the air bubbles. The alloy is poured into a casting mold and stirred with an admixture of 1.6 wt.% TiH₂ that is used as a blowing agent. Then, the foamed molten material is cooled down. A typical resulting internal structure of the aluminium foam is shown in Fig. 1(a).

Firstly, a large panel of Alporas (160 × 100 × 60 mm) was polished and scanned with a high resolution scanner. Acquired images were segmented to binary ones and further used in an image analysis. Then, a smaller Alporas block was cut into thin slices (~5 mm) and embedded into epoxy resin to fill the pores. The surface was mechanically grinded and polished to reach minimum surface roughness suitable for nanoindentation. Very low roughness $R_q \approx 10$ nm [15] was achieved on the cell walls. Then, the sample was investigated with electron microscopy and nanoindentation.

2.2. SEM and microstructural analysis

The microstructure of the cell walls was firstly studied in scanning electron microscope (SEM). It was found that a significant inhomogeneity of the microstructural material phases exists on the level of tens of micrometers (Fig. 1(b) and (c)). Two distinct phases, that exhibit different color in back-scattered electron (BSE) images, can be distinguished. The chemical composition of the two phases was checked with EDX element analysis in SEM. It was found that the majority of the volume (dark zone in Figs. 1(c) and 2(a)) consists of aluminium (~67 wt.%), oxygen (~32 wt.%), and further trace elements (Mg, Ti, Fe, Co, Ni, Cu, Si < 2 wt.%). Lighter zones in Fig. 2 consist of Al (~60 wt.%), O (~30 wt.%), Ca (~5 wt.%), Ti (~5 wt.%) and other elements (<1 wt.%). As expected, the majority of the volume (dark zone) is

composed of aluminium and aluminium oxide Al₂O₃ (further denoted as Al-rich area). Lighter zones contain significant amount of calcium and titanium (further denoted as Ca/Ti-rich area). The non-uniform distribution of these zones shows inhomogeneous mixing of the admixtures that are added during the production process.

2.3. Image analysis and porosity

In order to estimate the volume fractions of Al-rich and Ca/Ti-rich areas, image analysis based on previously taken SEM images was employed. Ten arbitrarily chosen areas on wall cross sections were explored. Images were segmented to two phases using a common threshold value of a grey level for all images (Fig. 2). The Ca/Ti-rich area was estimated to cover $22 \pm 4\%$ of the whole area.

The overall porosity of the sample was assessed by weighing of a large Alporas panel (knowing the sample dimensions and solid mass density 2700 kg m^{-3}). The porosity reached 91.4% which corresponds to e.g. [3,16]. In other words, solid mass (i.e. the cell walls) occupied only 8.6% of the total volume in the specimen.

Further, the distributions of the cell wall thicknesses and the distribution of pore sizes were studied by means of pore contour detection in the Matlab environment. At first, the contours were generated for every pore in the image and section properties (centroid, area, second moment of inertia) were computed (Fig. 3). The wall thicknesses were calculated as the minimum distance between the neighboring contours. The distribution of the thicknesses is shown in Fig. 4 where a significant peak occurs around ~60 μm which can be understood as a characteristic cell wall thickness.

Then, equivalent ellipses were constructed from contours under the condition that they have the same area and the same principal second moment of inertia. Such assumption led to the evaluation of two main half axes (a_i and b_i) for each equivalent ellipse. In order to characterize the shape of pores, an equivalent ellipse shape factor was defined as the ratio $e_i = \frac{a_i}{b_i}$. The distribution of the shape factor is depicted in Fig. 5. It can be concluded that pores have typically a round shape with the shape factor lying mostly between 1 and 2. The peak with the highest occurrence in Fig. 5 appears around $e_i = 1.15$.

Due to the round shape of pores, it also makes sense to compute an equivalent pore diameter using a circular pore replacement. The distribution of equivalent circular pores is depicted in Fig. 6. Wide distribution of pores with diameters 0–6 mm was found. The mean equivalent diameter was found to be 2.9 ± 1.5 mm for the specific specimen.

2.4. Nanoindentation

Micromechanical properties of the cell walls were measured by means of nanoindentation. The tests were performed using the

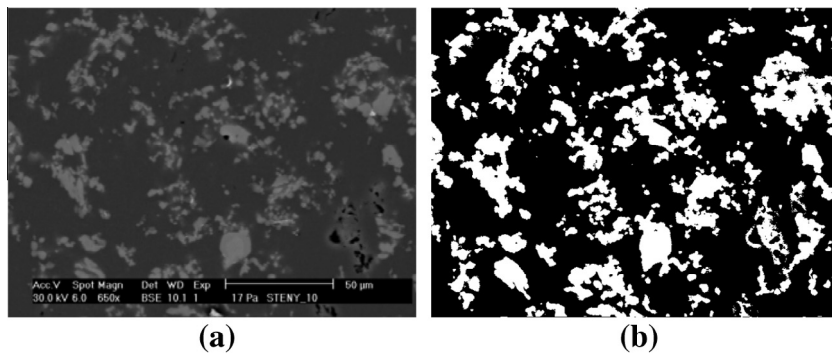


Fig. 2. An example of (a) SEM image of the cell wall and (b) processed image segmented to two phases (white = Ca/Ti-rich, black = Al-rich area).

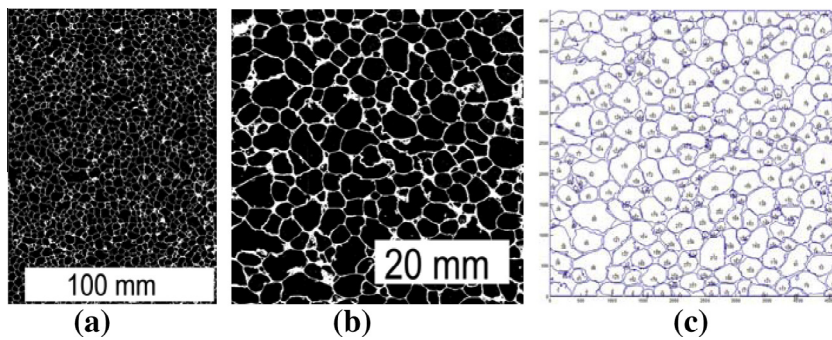


Fig. 3. (a) Binary image of the polished foam panel. (b) Binary image of $\sim 50 \times 50$ mm foam cut. (c) Cell contours in the cut (prepared in Matlab).

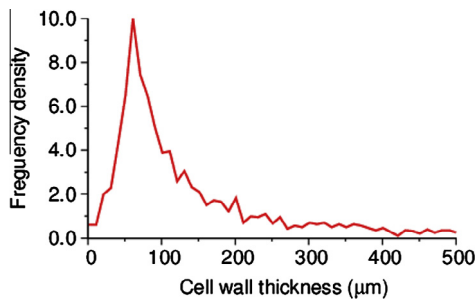


Fig. 4. Distribution of cell wall thicknesses.

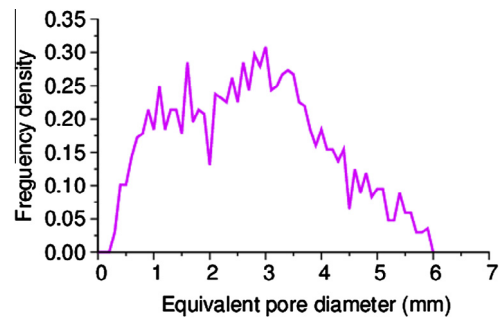


Fig. 6. Distribution of equivalent circular pores.

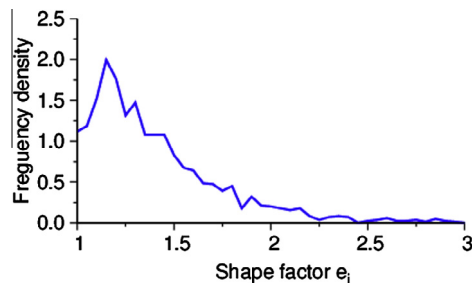


Fig. 5. Distribution of equivalent ellipse shape factor.

Hysitron Tribolab system[®] at the Czech Technical University in Prague. This system consists of in-situ SPM imaging which was used for scanning the sample surface. Three-sided pyramidal diamond tip (Berkovich type) was used for all measurements. Two distant locations were chosen on the sample to capture its heterogeneity. Each location was covered by a series of 10×10 indents

with $10 \mu\text{m}$ spacing (Fig. 7). It yields 200 indents in total which was considered to give sufficiently large statistical set of data. Standard load controlled test of an individual indent consisted of three segments: loading, holding at the peak and unloading. Loading and unloading of this trapezoidal loading function lasted for 5 s, the holding part lasted for 10 s. Maximum applied load was 1 mN. Maximum indentation depths were ranging between 100 and 300 nm depending on the stiffness of the indented phase. Elastic modulus was evaluated for individual indents using standard Oliver and Pharr methodology [17] which accounts for elasto-plastic contact of a conical indenter with an isotropic half-space as

$$E_r = \frac{1}{2\beta} \frac{\sqrt{\pi}}{\sqrt{A}} \frac{dP}{dh} \quad (1)$$

in which E_r is the reduced modulus measured in an experiment, A is the projected contact area of the indenter at the peak load, β is a

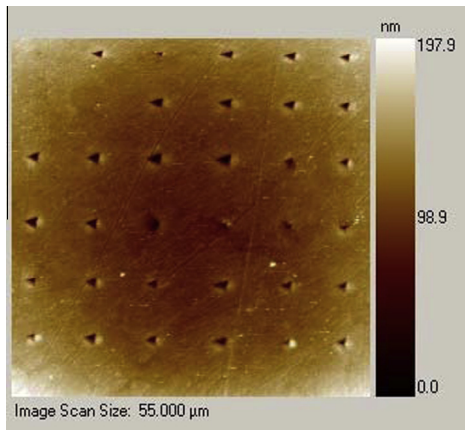


Fig. 7. Part of the indentation matrix showing 6 × 6 indents with 10 μm spacing as scanned with Hysitron Tribolab.

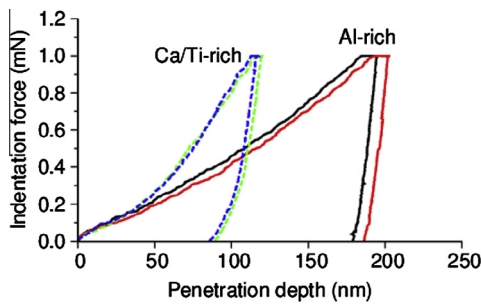


Fig. 8. Typical loading diagrams for Al-rich and Ca/Ti-rich zones.

geometrical constant ($\beta = 1.034$ for the used Berkovich tip) and $\frac{dF}{dh}$ is a slope of the unloading branch evaluated at the peak. Young's modulus E of the measured media can be found using contact mechanics which accounts for the effect of non-rigid indenter as

$$\frac{1}{E_r} = \frac{(1 - \nu^2)}{E} + \frac{(1 - \nu_i^2)}{E_i} \quad (2)$$

in which ν is the Poisson's ratio of the tested material, E_i a ν_i are known elastic modulus and Poisson's ratio of the indenter. In our case, $\nu = 0.35$ was taken as an estimate for all indents.

For the use of analytical homogenization techniques, the material was decomposed into individual phases using the statistical deconvolution technique [11–13]. It searches for n-Gauss distributions in an experimental probability density function – PDF (Fig. 9) of the analyzed quantity, i.e. elastic modulus in this case. Random seed and minimizing criteria of the differences be-

tween the experimental and theoretical overall PDFs (particularly quadratic norm of the differences) are computed in the algorithm to find the best fit. Details on the deconvolution technique can be found in [12,13]. Two-phase system (one dominant Al-rich phase and one minor Ca/Ti-rich phase) was assumed in our deconvolution which corresponds to SEM findings.

3. Numerical part

3.1. Scale separation

In order to describe heterogeneous systems and their effective properties, representative volume element (RVE) have been previously introduced [14]. RVE statistically represents a higher structural level of the material and serves for evaluation of the effective (homogenized) properties within the defined volume. It includes all microstructural inhomogeneities that should be substantially smaller than the RVE size. The definition of the material scales can be defined through the scale separation inequality:

$$s \ll V \ll D \quad (3)$$

in which s is the characteristic size of the largest microstructural inhomogeneity, V is the RVE size and D is a characteristic structural length scale. Knowing the material and geometrical properties of the microstructural material phases a homogenization can be performed.

Nanoindentation is able to access intrinsic material properties of individual micro-scale phases provided the dimension of an indent (h) is small enough, i.e. $h \ll s$. As a rule of thumb $h < s/10$ is usually used to access material properties of individual constituents without any dependence on the length scale.

As mentioned above, the metal foam material has a hierarchical microstructure. At least two levels need to be considered:

- **Level I** (the cell wall level) has a characteristic dimension defined by the mean midspan wall thickness $V_I \sim 60 \mu\text{m}$. This level consists of prevailing aluminium matrix (Al-rich area) with embedded heterogeneities in the form of Ca/Ti-rich areas. Intrinsic elastic properties of the constituents were assessed by nanoindentation at this level. Individual indent size was prescribed to be considerably smaller ($h \approx 100\text{--}300 \text{ nm}$) than a characteristic size of Ca/Ti inhomogeneities ($\sim 4 \mu\text{m}$).
- **Level II** (the foam level) has a characteristic dimension of $V_{II} \sim 50 \text{ mm}$. At this level, large pores with an average equivalent diameter $\sim 2.9 \text{ mm}$ (assuming circular pores) occur in the total volume of 91.4%. At Level II, the cell walls are considered as homogeneous having the properties that come from the Level I homogenization.

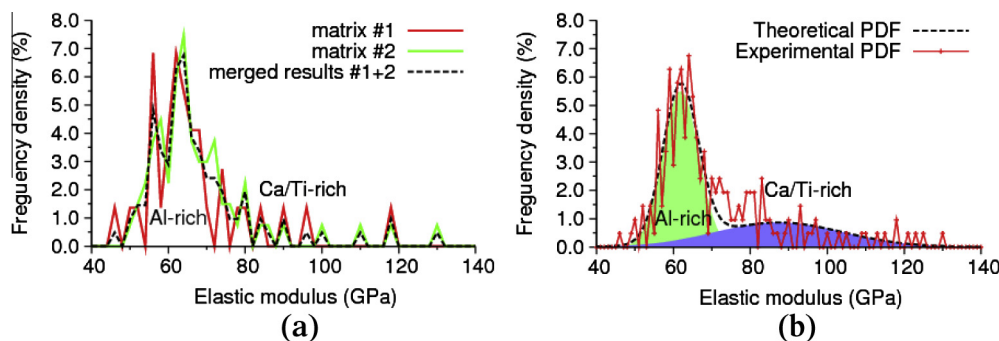


Fig. 9. (a) Probability density functions of elastic moduli from two measured positions and (b) merged results with deconvoluted phases.

3.2. Analytical homogenizations of Level I

The RVE with substantially smaller dimensions than the macro-scale body allows imposing homogeneous boundary conditions over the RVE. Continuum micromechanics provides a framework, in which elastic properties of heterogeneous microscale phases are homogenized to give overall effective properties on the upper scale [14]. A significant group of analytical homogenization methods relies on the Eshelby's solution [18] that is derived for ellipsoidal inclusions embedded in an infinite body. Then, uniform stress field appears in inclusions when macroscopic load is applied in infinity. Effective elastic properties are obtained through averaging over the local contributions.

From the material point of view, composite materials are usually characterized by a prevailing matrix phase, which serves as a reference medium in homogenization methods, reinforced with geometrically distinguishable inclusions. For example, the Mori–Tanaka method [19] can be appropriate for these cases. In this method, the effective bulk k_{eff} and shear μ_{eff} moduli of the composite with spherical inclusions are computed as follows

$$k_{eff} = \frac{\sum_r f_r k_r \left(1 + \alpha_0 \left(\frac{k_r}{k_0} - 1\right)\right)^{-1}}{\sum_r f_r \left(1 + \alpha_0 \left(\frac{k_r}{k_0} - 1\right)\right)^{-1}}, \quad (4)$$

$$\mu_{eff} = \frac{\sum_r f_r \mu_r \left(1 + \beta_0 \left(\frac{\mu_r}{\mu_0} - 1\right)\right)^{-1}}{\sum_r f_r \left(1 + \beta_0 \left(\frac{\mu_r}{\mu_0} - 1\right)\right)^{-1}}, \quad (5)$$

$$\alpha_0 = \frac{3k_0}{3k_0 + 4\mu_0}, \quad \beta_0 = \frac{6k_0 + 12\mu_0}{15k_0 + 20\mu_0}, \quad (6)$$

where f_r is the volume fraction of the r th phase, k_r its bulk modulus and the coefficients α_0 and β_0 describe bulk and shear properties of the 0th phase, i.e. the reference reference medium [19,14]. The bulk and shear moduli can be directly linked with Young's modulus E and Poisson's ratio ν used in engineering computations as

$$E = \frac{9k\mu}{3k + \mu}, \quad (7)$$

$$\nu = \frac{3k - 2\mu}{6k + 2\mu}. \quad (8)$$

Polycrystalline metals, in which no preference of matrix phase exists, are usually modeled with the self-consistent scheme [14] in which the reference medium refers back to the homogenized medium itself. Regardless the most suitable homogenization technique, which would be probably the Mori–Tanaka method in our case, we use multiple estimates assuming spherical inclusions. Namely, the Mori–Tanaka method, self-consistent scheme, Voigt and Reuss bounds.

As a first step, we use analytical schemes to predict characteristic effective properties on the Level I and thus characteristic phase values need to be identified at first. We propose to use grid nano-indentation and statistical deconvolution of the phase properties to solve this task which leads to the assessment of phase distributions for their elastic properties. Although, it would be possible to perform a probabilistic computation with these results (as described e.g. in [20]), and to find fluctuations of the effective properties in the analytical solutions we leave the calculation as deterministic and we concentrate on the validation of the homogenization by numerical (FFT-based) method which fully respects the spatial distribution of material heterogeneities without any geometrical restrictions.

3.3. Numerical homogenization of Level I based on FFT

In order to verify results from simple analytical schemes, advanced homogenization method based on fast Fourier transformation (FFT) was used. The behavior of any heterogeneous materials consisting of periodically repeating RVE (occupying domain $\Omega = \prod_{i=1}^d (-Y_i, Y_i)$, where Y_i is the axial size and d denotes the space dimension) can be described with differential equations with periodic boundary conditions and prescribed macroscopic load as

$$\langle \boldsymbol{\varepsilon} \rangle := \frac{1}{|\Omega|} \int_{\Omega} \boldsymbol{\varepsilon}(\mathbf{x}) d\mathbf{x} = \boldsymbol{\varepsilon}^0, \quad (9)$$

$$\boldsymbol{\sigma}(\mathbf{x}) = \mathbf{L}(\mathbf{x}) : \boldsymbol{\varepsilon}(\mathbf{x}) \quad \text{div } \boldsymbol{\sigma}(\mathbf{x}) = \mathbf{0} \quad \mathbf{x} \in \Omega, \quad (10)$$

where $\boldsymbol{\sigma}$ denotes symmetric second order stress tensor, $\boldsymbol{\varepsilon}$ symmetric second order strain tensor and $\mathbf{L}(\mathbf{x})$ the fourth order tensor of elastic stiffness at individual locations \mathbf{x} . The effective (homogenized) material tensor \mathbf{L}_{eff} is such a tensor satisfying

$$\langle \boldsymbol{\sigma} \rangle = \mathbf{L}_{eff} \langle \boldsymbol{\varepsilon} \rangle \quad (11)$$

for an arbitrary macroscopic strain $\boldsymbol{\varepsilon}^0 = \langle \boldsymbol{\varepsilon} \rangle$. Thus the problem of finding effective material tensor is composed of finding corresponding strain field $\boldsymbol{\varepsilon}$ and associated stress field $\boldsymbol{\sigma}$ for known elastic properties \mathbf{L} and prescribed strain $\boldsymbol{\varepsilon}^0$ using differential Eq. (10).

In addition to discretization of the weak formulation leading to classical finite element method, the problem can be solved by method based on the fast Fourier transform, proposed by Moulinec and Suquet in [22], based on an integral (Lippmann–Schwinger) equation

$$\boldsymbol{\varepsilon}(\mathbf{x}) + \int_{\Omega} \Gamma^0(\mathbf{x} - \mathbf{y}) : (\mathbf{L}(\mathbf{y}) - \mathbf{L}^0) : \boldsymbol{\varepsilon}(\mathbf{y}) d\mathbf{y} = \boldsymbol{\varepsilon}^0, \quad (12)$$

where Γ^0 is the periodic Green's operator associated with the reference elasticity tensor \mathbf{L}^0 which is a parameter of the method. The operator is expressed in the Fourier space as

$$\begin{aligned} \hat{\Gamma}_{ijkl}^0(\boldsymbol{\xi}) &= \frac{1}{4\mu|\boldsymbol{\xi}|^2} (\delta_{ki}\xi_l\xi_j + \delta_{il}\xi_k\xi_j + \delta_{ij}\xi_l\xi_k + \delta_{ij}\xi_k\xi_l) \\ &\quad - \frac{\lambda + \mu}{\mu(\lambda + 2\mu)} \frac{\xi_i\xi_j\xi_k\xi_l}{|\boldsymbol{\xi}|^4}. \end{aligned} \quad (13)$$

The numerical solution of Eq. (13) is based on the discretization of the periodic unit cell Ω (PUC) into a regular periodic grid with $N_1 \times \dots \times N_d$ nodal points and grid spacings $\mathbf{h} = (2\frac{Y_1}{N_1}, \dots, 2\frac{Y_d}{N_d})$. The searched field $\boldsymbol{\varepsilon}$ is approximated by a trigonometric polynomial \mathbf{e}_N in the form [23]

$$\mathbf{e}(\mathbf{x}) \approx \mathbf{e}_N(\mathbf{x}) = \sum_{\mathbf{k} \in Z_N^d} \hat{\mathbf{e}}(\mathbf{k}) \varphi_{\mathbf{k}}(\mathbf{x}), \quad \mathbf{x} \in \Omega, \quad (14)$$

where $\mathbf{N} = (N_1, \dots, N_d)$, $\hat{\mathbf{e}}$ designates the Fourier coefficients and

$$Z_N^d = \left\{ \mathbf{k} \in Z^d : -\frac{N_\alpha}{2} \leq k_\alpha < \frac{N_\alpha}{2}, \alpha = 1, \dots, d \right\}. \quad (15)$$

The discretization leads to a non-symmetric linear system of equations

$$[\mathbf{I} + \mathbf{F}^{-1} \hat{\Gamma} \mathbf{F} (\mathbf{L} - \mathbf{L}^0)] \mathbf{e} = \mathbf{e}^0, \quad (16)$$

where the vector \mathbf{e} stores a strain field at discretization points and \mathbf{e}^0 the macroscopic strain, \mathbf{L} and \mathbf{L}^0 stores the material coefficients at discretization points and reference elasticity tensor respectively, \mathbf{I} denotes the identity matrix, $\hat{\Gamma}$ stores the values corresponding to the integral kernel in the Fourier space, and \mathbf{F} (\mathbf{F}^{-1}) stores the (inverse) discrete Fourier transform matrices that can be provided by the fast Fourier transform algorithm. The possibility to solve the non-symmetric linear system by the conjugate gradient method is proposed by Zeman et al. in [24] and justified in Vondřejc et al.

[25], where also the particular expression of individual matrices can be found for the problem of electric conductivity or heat transfer. The linear system (Eq. (16)) depends only on stiffness coefficients at grid points that can be obtained using nanoindentation and thus the homogenized (effective) tensor $\mathbf{L}_{\text{eff}}^{\text{FFT}}$ can be calculated from Eq. (11). The particular case of homogenization of elastic properties received from nanoindentation on a sample surface (half-space) also requires an assumption of plane strain conditions.

The resulting homogenized stiffness tensor $\mathbf{L}_{\text{eff}}^{\text{FFT}}$ must be symmetric, positive definite, but generally it is anisotropic even for isotropic phases. The resulting anisotropy of the tensor depends on the topology of phases (or inclusions) in the PUC. Note also, that the FFT homogenization takes no assumptions on the geometry of the phases as in the case of analytical schemes. It uses only the stiffness coefficients distributed within the PUC and its accuracy depends only on the density of the grid points, i.e. nanoindentation grid points in our case.

3.4. Comparison of analytical and numerical schemes

The comparison of the analytical and the FFT schemes includes an assessment of the stiffness matrix (here in Mandel's notation) for isotropic material assuming plane strain conditions (equally with the FFT scheme) as

$$\mathbf{L}_{\text{eff}}^{\text{A}} = \frac{E_{\text{eff}}}{(1 + \nu_{\text{eff}})(1 - 2\nu_{\text{eff}})} \begin{bmatrix} 1 - \nu_{\text{eff}} & \nu & 0 \\ \nu & 1 - \nu_{\text{eff}} & 0 \\ 0 & 0 & 1 - 2\nu_{\text{eff}} \end{bmatrix}, \quad (17)$$

where E_{eff} and ν_{eff} comes from analytical methods.

The difference between the analytical results ($\mathbf{L}_{\text{eff}}^{\text{A}}$) and numerically computed stiffness matrix ($\mathbf{L}_{\text{eff}}^{\text{FFT}}$) can be expressed using a stiffness error metric as

$$\delta(\mathbf{L}_{\text{eff}}^{\text{FFT}}, \mathbf{L}_{\text{eff}}^{\text{A}}) = \sqrt{\frac{(\mathbf{L}_{\text{eff}}^{\text{FFT}} - \mathbf{L}_{\text{eff}}^{\text{A}}) :: (\mathbf{L}_{\text{eff}}^{\text{FFT}} - \mathbf{L}_{\text{eff}}^{\text{A}})}{(\mathbf{L}_{\text{eff}}^{\text{FFT}} :: \mathbf{L}_{\text{eff}}^{\text{FFT}})}}. \quad (18)$$

We also define an anisotropy degree of stiffness matrix ($\mathbf{L}_{\text{eff}}^{\text{FFT}}$) as

$$\rho(\mathbf{L}_{\text{eff}}^{\text{FFT}}) = \inf_{\mathbf{L}_{\text{iso}} - \text{isotropic matrix}} \delta(\mathbf{L}_{\text{eff}}^{\text{FFT}}, \mathbf{L}_{\text{iso}}). \quad (19)$$

It measures the distance between $\mathbf{L}_{\text{eff}}^{\text{FFT}}$ and all isotropic matrices – the calculation is provided analytically as the metric is dependent only on two material constants. We also note that the degree of anisotropy is zero for an isotropic matrix.

4. Results and discussion

4.1. Nanoindentation

Results from nanoindentation clearly indicated heterogeneity of the cell walls, i.e. the presence of mechanically different inclusions. An example of typical loading diagrams gained from nanoindentation at Al-rich area (dark zone in Fig. 1(b) and (c)) and Ca/Ti-rich area (light zone in Fig. 1(b) and (c)) are shown in Fig. 8. Due to the load controlled nanoindentation test, the final penetration depth varied for differently stiff phases. An average maximum depth of penetration reached by the indenter was around ~180 nm. Higher values (~190 nm) were reached for more compliant Al-rich zone whereas the indentation depths to harder but less frequent Ca/Ti-rich areas were around 100 nm.

Elastic moduli were evaluated for each individual indent. Overall results are depicted in Fig. 9(a) plotting histogram of all elastic moduli obtained from two different positions and the results merged from both positions. No significant differences between

the positions were found. Therefore, merged results were further used in the deconvolution of phase elastic properties.

Two-phase system (one dominant Al-rich phase and one minor Ca/Ti-rich phase) was assumed in the deconvolution algorithm (Fig. 9(b)). It can be seen in Fig. 9(b) that a significant peak appears around 62 GPa. This value can be considered as a dominant characteristic of the prevailing phase (Al-rich). The rest of the results can be attributed to the minor Ca/Ti-rich phase. Table 1 contains numerical results from the deconvolution with the estimated volume fractions of the phases.

The characteristic value for the first phase roughly corresponds to the elastic modulus of pure aluminium (70 GPa, Ref. [21]). The lower value obtained from nanoindentation suggests that probably some small-scale porosity or impurities (Ca) added to the molten are intrinsically included in the results of this mechanically dominant phase. The determined elastic modulus of Al-rich zone is also in excellent agreement with the value 61.7 GPa measured by Jeon et al. [6] on melted Al-1.5 wt.%Ca alloy.

4.2. Level I homogenization

It is clear from SEM images (Figs. 1 and 2) that the Ca/Ti-rich areas occupy much larger space of the solid compared to the initial batch volume fractions (Ca and TiH₂ content is less than 1 vol.%). Chemical reactions and precipitation during hardening form new compounds in the Al matrix. It follows from other studies [7,26] that zones formed by precipitates of Al₄Ca and TiAl₃ develop in the metal solid. The volume of these Ca/Ti-rich areas in the sample was estimated by image analysis from segmented SEM images as 22 ± 4%. Results from statistical nanoindentation (36.2%) suggest that a substantially larger part of the matrix is mechanically influenced by the Ca/Ti addition and a higher fraction of the volume belongs to this mechanically distinct phase.

The elastic homogenization of the Level I was performed considering input parameters from nanoindentation. In Table 2, the homogenized elastic moduli are summarized for individual homogenization techniques. Very close bounds and insignificant differences in the estimates given by the schemes were found. In the following considerations, we use the result received from the Mori–Tanaka scheme, i.e. we take the homogenized isotropic elastic constants (Young's modulus and Poisson's ratio) of the Level I as $E_{\text{eff},I} = 70.083$ GPa, $\nu_{\text{eff},I} = 0.35$.

Further, numerical FFT-based homogenization algorithm was applied and the stiffness matrix was computed from grid values of elastic moduli obtained in nanoindentation.

The resulting stiffness matrices (in Mandel's notation) computed from analytical Mori–Tanaka results (i.e. using Eqs. (4)–(8)) and from FFT homogenization are:

$$\mathbf{L}_{\text{eff}}^{\text{A}} = \begin{bmatrix} 112.479 & 60.566 & 0 \\ 60.566 & 112.479 & 0 \\ 0 & 0 & 51.913 \end{bmatrix} \text{ (GPa)}, \quad (20)$$

$$\mathbf{L}_{\text{eff}}^{\text{FFT}} = \begin{bmatrix} 117.1300 & 62.7413 & -0.1625 \\ 62.7413 & 117.1060 & -0.1430 \\ -0.1625 & -0.1430 & 54.3132 \end{bmatrix} \text{ (GPa)}. \quad (21)$$

Table 1
Elastic moduli and volume fractions from deconvolution.

| Phase | Mean (GPa) | St. dev. (GPa) | Volume fraction (-) |
|---------------------|------------|----------------|---------------------|
| 1 (Al-rich zone) | 61.88 | 4.6 | 0.638 |
| 2 (Ca/Ti-rich zone) | 87.40 | 16.7 | 0.362 |

Table 2
Values of the Level I effective Young's modulus computed by different homogenization schemes.

| Scheme | Mori–Tanaka | Self-consist. scheme | Voigt bound | Reuss bound |
|---------|-------------|----------------------|-------------|-------------|
| E (GPa) | 70.083 | 70.135 | 71.118 | 69.195 |

It is worth noting that the analytical form of the stiffness matrix $\mathbf{L}_{\text{eff}}^A$ as well as $\mathbf{L}_{\text{eff}}^{\text{FFT}}$ contains perfect symmetry by definition. The stiffness error evaluated for the matrices by Eq. (18) is $\delta = 0.0393$. The difference in schemes less than 4% shows a very good agreement of the methods for the studied case.

The $\mathbf{L}_{\text{eff}}^{\text{FFT}}$ matrix is characterized by a very small degree of anisotropy ($\rho = 0.0016$, Eq. (19)). The nonzero value is caused mainly by the fact that microstructural phases are not absolutely uniformly dispersed within the tested volume. However, the anisotropy is very small. Consequently, this finding also justifies the usage of analytical methods producing isotropic effective (homogenized) properties. Note also, that negative components appearing in $\mathbf{L}_{\text{eff}}^{\text{FFT}}$ are in no discrepancy with physical meaning (only the positive definiteness is required). They are just a product of the small anisotropy.

4.3. Level II homogenization

At this level, cell walls are considered as a homogeneous phase having the properties that come from the Level I homogenization. The solid phase is very sparse in the sample volume due to its porosity (91.4% of air). The walls create a matrix phase and the large air pores can be considered as inclusions with zero stiffness in this homogenization.

Since analytical approaches are often used also for extreme cases of large stiffness contrast of phases or for large sample porosities (e.g. [27]), we firstly tried to estimate effective elastic properties with the same analytical schemes used at Level I. The result is summarized in Table 3. Voigt and Reuss bounds are quite distant in this case. Unfortunately, simple analytical schemes also fail to predict correctly the composite stiffness due to the extreme sample porosity. The Mori–Tanaka method approaches the arithmetic mean between the bounds, whereas the self-consistent scheme tends to reach the stiffness of the phase with higher occurrence (i.e. the air).

Most of analytical studies on the homogenization of foams are based on models with a regular periodic microstructure [28,29]. Nevertheless, real foam microstructures are characterized with different sizes and shapes and sizes of pores rather than with periodic structures as shown in Section 2 of this paper. The solution can be to solve the problem of irregular microstructures by an analysis of a large representative volume element containing large enough number of pores. Such model can be solved in two or three dimensions.

Therefore, more appropriate (but still simple) two dimensional microstructure based FEM model was proposed. The model geometry was generated from high resolution optical image of polished foam cross-section (Fig. 10(a)). Square domain with 106×106 mm size (i.e. being much larger than an average pore size ~ 2.9 mm)

Table 3
Values of the Level II effective Young's modulus computed by different analytical homogenization schemes.

| Scheme | Mori–Tanaka | Self-consist. scheme | Voigt bound | Reuss bound |
|---------|-------------|----------------------|-------------|-------------|
| E (GPa) | 3.1510 | 0.0012 | 6.0200 | 0.0011 |

was extracted from the image. At this domain, pore centroids were detected, Delaunay triangulation applied and Voronoi cells created. Then, an equivalent 2D-beam structure was generated from Voronoi cell boundaries (Fig. 10(b)). Based on several numerical studies performed for this purpose (but not shown here in details), it was found that the distribution of cross sectional areas and bending stiffness of individual beams do not play a significant role in the evaluation of the homogenized elastic properties. The overall stiffness is influenced mainly by the sum of the beam cross sectional areas and by the beam inclination to the load direction. The contribution of the beam bending stiffness is diminished due to the very large beam length compared to its small cross sectional dimensions. Therefore, as an approximate but sufficient estimate, uniform cross-sectional area and uniform second moment of inertia were prescribed to all beams. The beam cross sectional area (A_{beam}) was computed from the total sample porosity ($\varphi = 0.086$) and the total length of all beams (l_{total}) in the RVE with rectangular dimensions $a \times b$ as

$$A_{\text{beam}} = \frac{ab\varphi}{l_{\text{total}}} \quad (22)$$

Taking into account 2-D case (i.e. unit thickness of the plane) beam height can be set as

$$h_{z,\text{beam}} = \frac{A_{\text{beam}}}{1} = A_{\text{beam}} \quad (23)$$

Assuming rectangular shape of a cross section one can readily obtain the second moment of inertia as

$$I_{y,\text{beam}} = \frac{1}{12} 1h_{z,\text{beam}}^3 = \frac{A_{\text{beam}}^3}{12} \quad (24)$$

In the analysis, macroscopic strain ϵ^0 is prescribed to the RVE and microscopic strains and stresses are solved. Volumetric averaging of microscopic stresses leads to the assessment of an average macroscopic stress and finally estimation of effective stiffness parameters. The key issue of the computation is the size of the RVE and application of boundary conditions around the domain. Since the domain size is always smaller than an infinite body, any constraints can strongly influence the results. Application of the kinematic boundary conditions leads to the overestimation of effective stiffness and it can give an upper bound, whereas the static boundary conditions give a lower bound [30]. The best solution is usually provided by applying periodic boundary conditions to RVE which are, however, difficult to implement into commercial codes.

Nevertheless, the influence of the boundary conditions on microscopic strains and stresses in the domain decrease in distant points from the boundary. The size of our domain (106×106 mm) allowed us to solve the problem with kinematic boundary conditions. For homogenization, considerably smaller region (later found optimum 35–50 mm) in the central part was used. Microscopic strains and stresses were computed inside this smaller area which was assumed to be still sufficiently large to describe the material inhomogeneities and to serve as the material RVE.

Kinematic constraints were applied on all domain sides. Free beams located around the boundary and not connected to any cell were deleted and supports put on the nodes located on the closest cell. Such arrangement of beams and supports prevented the structure from unreasonably large deformations of these free boundary beams. Finally, the FE model consisted of 2117 nodes and 3099 beam elements.

The elastic analysis was performed on the whole domain (106×106 mm) subjected to homogeneous macroscopic strain in one axial direction ($\epsilon^0 = \{1, 0, 0\}^T$) by imposing prescribed displacement to one domain side (Fig. 10(c)). In general, compressive mechanical properties of the foam are not equal to tensile properties results beyond the elastic limit. In our case, however, the

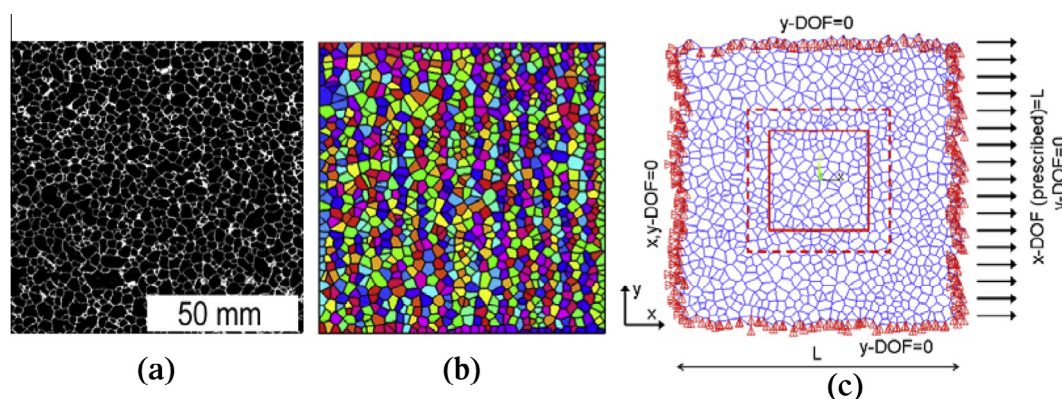


Fig. 10. (a) Binary image of the foam (106 × 106 mm). (b) Voronoi tessellation. (c) 2-D beam model with boundary constraints (red squares indicate optimum RVE sizes from which homogenized properties have been obtained; solid line = 35 × 35 mm, dashed line = 50 × 50 mm).

homogenized elastic modulus (i.e. using elastic solution only) will be the same for both tension (as in the model) and compression (which was later used in our experimental program). The test was performed using commercial Ansys FEM software and microscopic strains and stresses solved in the domain. Strains and stresses (structural forces for the case of beams, respectively) inside the smaller area (35–50 mm) were averaged and used for computation of the homogenized stiffness matrix (one column in the matrix, respectively). Assuming material isotropy, the first component (1,1) at the material stiffness matrix is given by:

$$L_{11} = E \frac{(1 - \nu)}{(1 + \nu)(1 - 2\nu)} \quad (25)$$

in which E is the Young's modulus and ν Poisson's ratio, respectively. Since the Poisson's ratio of the whole foam is close to zero (as confirmed by experimental measurements) the L_{11} member coincides with the Young's modulus E .

For the tension test in x -direction (Fig. 10(c)), the homogenized Young's modulus was found to be RVE size dependent. Experimental investigations of the dependence of sample size on apparent elastic modulus and strength were conducted e.g. by Ashby et al. [31]. They found, the modulus and strength become independent of size when the sample dimensions exceeded about seven cell diameters. This would imply minimum RVE size 20.3 mm for our typical cell size (2.9 mm). On the other hand, the RVE size should not exceed roughly 1/3 to 1/2 of the whole domain size not to be influenced by boundary conditions which implies maximum RVE width about 35 to 53 mm for our 106 mm wide domain. To find an optimum RVE size a numerical study was conducted for different RVE sizes in the range 20 to 90 mm (see Fig. 11). An optimum RVE was confirmed to be between 35 and 50 mm for our specific domain. Results for smaller RVEs (<35 mm) are influenced by the beam inhomogeneity inside the RVE (in other words, such small RVE is not representative enough) whereas larger RVEs (>50 mm) are already influenced by the vicinity of boundary conditions. For optimum RVE sizes, the effective Young's modulus varied in the range $E_{eff,II} = 1.36\text{--}1.38$ GPa.

The resulting homogenized Young's modulus is comparable with the range of experimental values reported for Alporas® e.g. by Ashby et al. [31] (0.4–1 GPa), Sugimura et al. [7] (1.05–1.25 GPa) or Simone et al. [26] (0.87–1.21 GPa).

Experimental measurements in uniaxial compression performed on our samples (30 × 30 × 60/90 mm Alporas blocks) indicate $E = 1.45 \pm 0.15$ GPa (see Section 4.4). The slightly lower stiffness obtained from the proposed two-dimensional model can be explained by the lack of additional confinement appearing in the three-dimensional case and the simplified beam geometry.

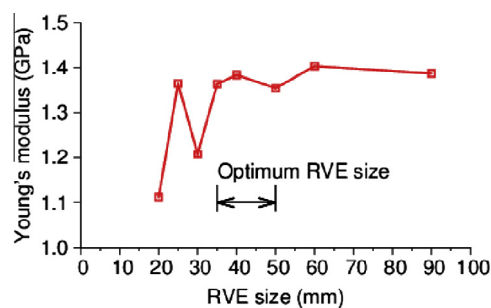


Fig. 11. Dependence of effective Level II Young's modulus on RVE size.

The influence of the RVE size can also play a role as described above. However, the obtained difference is small (~5%), probably also due to the almost zero foam Poisson's ratio. Anyway, results of the simplified 2-D model have to be treated as a relatively close but only the first estimate of the Level II material properties which should be refined e.g. by using more precise geometrical description or using a three-dimensional model.

4.4. Results from macroscopic measurements

Uniaxial compression tests on 30 × 30 × 60 and 30 × 30 × 90 mm Alporas blocks (Fig. 12(a)) were performed in an electromechanical press to verify numerical results on the Level II. Specimens were loaded-unloaded by five to ten cycles at very low strains and then fully compressed up to ~5% longitudinal strain (Fig. 12(b) and (c)). Longitudinal and transversal (engineering) strains were evaluated by means of digital image correlation (DIC) from CCD camera images taken during the test [32]. Negligible differences have been found between the slopes of loading/unloading cycles (Fig. 12(c)) which justifies evaluation of the elastic properties from this part of the loading diagram. Young's modulus was finally computed as the average slope from all relevant cycles (i.e. all cycles except the first and the last one that both can be influenced by non-linear effects). Young's modulus was determined as $E = 1.45 \pm 0.15$ GPa on six foam samples. Poisson's ratio was found to be $\nu \approx 0$ in the elastic regime.

It is worth noting that the elastic limit of the foam lies in very low strains since local yielding and buckling of the thin corrugated walls starts early after the first loading. The elastic modulus assessment, therefore, requires high resolution of strain measurements not influenced by boundary conditions which might be difficult to obtain in classical test instrumentation (using e.g. tensometric

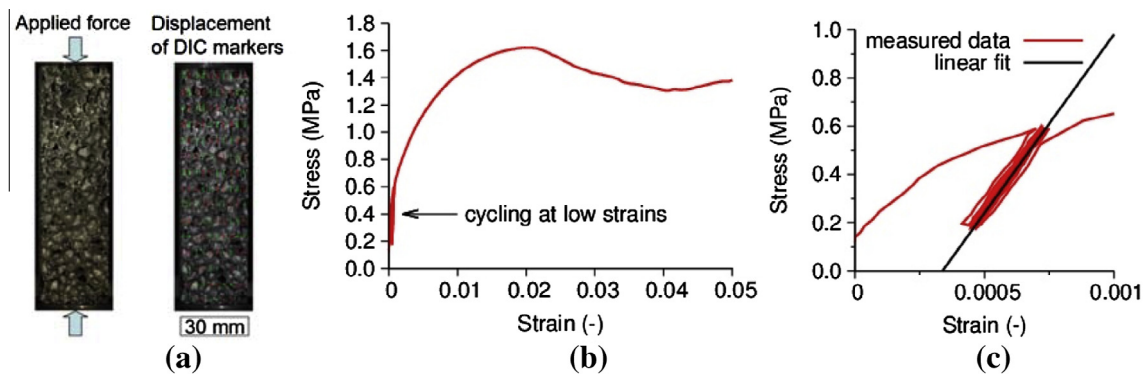


Fig. 12. Compression test. (a) Foam sample and an image with digital image correlation markers, (b) stress strain diagram, (c) detail of loading–unloading cycles at low strains.

gauges fixed to the sample, to the machine platens or using the cross-beam deflection). Some of the experimental results found in the literature, e.g. [33,34], use unloading modulus computed from an unloading cycle performed at approximately 75% of the peak stress (i.e. already after the yielding onset) rather than the initial modulus. However, such unloading modulus is not equivalent to the initial one. The DIC method provides an advantage of high precision also for strains about 10^{-6} . Thus, it is a suitable technique for the determination of the initial elastic modulus.

5. Conclusions

In this paper, a simple but effective two-scale microstructure based model of closed-cell aluminium foam was proposed to assess the homogenized elastic properties. The homogenization was split into two levels. The first one, characterized by thin cell walls ($\sim 60 \mu\text{m}$), was successfully homogenized with several analytical continuum mechanics schemes. Two different material phases (Al-rich and Ca/Ti-rich) were detected at this lower scale by SEM and statistical grid nanoindentation. Effective Young's modulus $E_{eff,I} \approx 70 \text{ GPa}$ was received regardless of the used scheme. The value was also justified by numerical FFT-based homogenization with a very good agreement (error less than 4%).

The upper foam level (Level II) contains homogenized walls and large air pores. Here, analytical tools were applied without success. Very poor estimates were given by the Mori–Tanaka or self-consistent schemes due to extremely high air content in the foam and large stiffness contrast. To better describe the real foam microstructure, a FEM model was proposed for the numerical homogenization at the second level. The model geometry was generated from large optical scan of polished foam cross section converted to the binary image. Delaunay triangulation and Voronoi tessellation have been applied and equivalent 2-D beam structure generated. The dependence of RVE size was solved in a large domain ($106 \times 106 \text{ mm}$) supported by kinematic boundary conditions. An optimum RVE size was found to be in the range 35–50 mm (i.e. 33–47% of the domain size) for which effective elastic properties were assessed ($E_{eff,II} = 1.36\text{--}1.38 \text{ GPa}$).

The model has proven to realistically describe macroscopic elastic properties of the foam. The two-dimensional approximation slightly underestimated the experimentally obtained stiffness ($E \approx 1.45 \text{ GPa}$). It is likely due to the inability to capture additional confinement coming from the three-dimensional material microstructure and the simplified beam geometry. Other possible reasons can lie in uncertainties connected with the foam geometrical representation, finite element discretization and boundary conditions applied in the homogenization. Nevertheless,

the prediction of elastic properties complies with the experimental results.

Further enhancement of the numerical model and generation of the model geometry from micro-CT data (i.e. extension to 3-D) are planned as future developments.

Acknowledgments

Financial support of the Czech Science Foundation is gratefully acknowledged (projects P105/12/0824 and P105/12/0331).

References

- [1] Němeček J, Králík V. A two-scale micromechanical model for closed-cell aluminium foams. In: Topping BHV, editor. Proceedings of the 11th international conference on computational structures technology. Stirlingshire, UK: Civil-Comp Press; 2012. <http://dx.doi.org/10.4203/ccp.99.259> [Paper 259].
- [2] Banhart J. Manufacture, characterisation and application of cellular metals and metal foams. *Prog Mater Sci* 2001;46:559–632.
- [3] Miyoshi T, Itoh M, Akiyama S, Kitahara A. Aluminium foam “ALPORAS”: the production process, properties and application. In: Materials Research Society Symp. Proc., vol. 521; 1998.
- [4] Hasan MA, Kim A, Lee H-J. Measuring the cell wall mechanical properties of Al-alloy foams using the nanoindentation method. *Compos Struct* 2008;83:180–8.
- [5] Papadopoulos DP, Konstantinidis IC, Papanastasiou N, Skolianos S, Lefakis H, Tsipas DN. Mechanical properties of Al metal foams. *Mater Lett* 2004;58(21):2574–8.
- [6] Jeon I et al. Cell wall mechanical properties of closed-cell Al foam. *Mech Mater* 2009;41(1):60–73.
- [7] Sugimura Y, Meyer J, He MY, Bart-Smith H, Grenstedt J, Evans AG. On the mechanical performance of closed cell Al alloy foams. *Acta Mater* 1997;45:5245–59.
- [8] Idris MI, Vodenitcharova T, Hoffman M. Mechanical behaviour and energy absorption of closed-cell aluminium foam panels in uniaxial compression. *Mater Sci Eng A* 2009;517:37–45.
- [9] Yongliang M, Guangchun Y, Hongjie L. Effect of cell shape anisotropy on the compressive behavior of closed-cell aluminum foams. *Mater Des* 2010;31:1567–9.
- [10] De Giorgi M, Carofalo A, Dattoma V, Nobile R, Palano F. Aluminium foams structural modelling. *Comput Struct* 2010;88:25–35.
- [11] Constantinides G, Chandran FR, Ulm F-J, Vliet KV. Grid indentation analysis of composite microstructure and mechanics: principles and validation. *Mater Sci Eng A* 2006;430(1–2):189–202.
- [12] Němeček J. Nanoindentation based analysis of heterogeneous structural materials. In: Němeček J, editor. Nanoindentation in materials science, ISBN: 978-953-51-0802-3, InTech; 2012. doi: <http://dx.doi.org/10.5772/50968>. Available from: <http://www.intechopen.com/books/nanoindentation-in-materials-science/nanoindentation-based-analysis-of-heterogeneous-structural-materials>.
- [13] Němeček J, Šmilauer V, Kopecký L. Nanoindentation characteristics of alkali-activated aluminosilicate materials. *Cem Concr Compos* 2011;33(2):163–70.
- [14] Zaoui A. Continuum micromechanics: survey. *J Eng Mech* 2002;128.
- [15] ISO 4287-1997, Geometrical Product Specifications (GPS) – surface texture: profile method – terms, definitions and surface texture parameters.
- [16] Ashby MF et al. Metal foams: a design guide. Elsevier; 2000.

- [17] Oliver W, Pharr GM. An improved technique for determining hardness and elastic modulus using load and displacement sensing indentation experiments. *J Mater Res* 1992;7(6):1564–83.
- [18] Eshelby JD. The determination of the elastic field of an ellipsoidal inclusion and related problem. *Proc R Soc Lond A* 1957;241:376–96.
- [19] Mori T, Tanaka K. Average stress in matrix and average elastic energy of materials with misfitting inclusions. *Acta Metall* 1973;21(5):571–4.
- [20] Kaminski M. *Computational mechanics of composite materials*. London: Springer; 2005.
- [21] Webelements on-line library. <http://www.webelements.com/aluminium/physics.html>.
- [22] Moulinec H, Suquet P. A fast numerical method for computing the linear and nonlinear mechanical properties of composites. *CR Acad Sci Sér II Méc Phys Chim Astron* 1994;318(11):1417–23.
- [23] Vainikko G. Fast solvers of the Lippmann–Schwinger equation. In: Gilbert RP, Kajiwara J, Xu YS, editors. *Direct and inverse problems of mathematical physics in international society for analysis. Applications and computation*. Dordrecht, The Netherlands: Kluwer Academic Publishers; 2000. p. 423–40.
- [24] Zeman J, Vondřejc J, Novák J, Marek I. Accelerating a FFT-based solver for numerical homogenization of periodic media by conjugate gradients. *J Comput Phys* 2010;229(21):8065–71.
- [25] Vondřejc J, Zeman J, Marek I. Analysis of a fast Fourier transform based method for modeling of heterogeneous materials. *Lect Notes Comput Sci* 2012;7116: 512–22.
- [26] Simone AE, Gibson LJ. Aluminum foams produced by liquid-state processes. *Acta Mater* 1998;46(9):3109–23.
- [27] Šejnoha M, Šmilauer V, Němeček J, Kopecký L. Application of micromechanics in engineering practice. In: Topping BHV, editor. *Proceedings of the eighth international conference on engineering computational technology*. Stirlingshire, Scotland: Civil-Comp Press; 2012.
- [28] Gibson LJ, Ashby MF. *Cellular solids: structure and properties*. Cambridge University Press; 1999.
- [29] Hohe J, Becker W. A probabilistic approach to the numerical homogenization of irregular solid foams in the finite strain regime. *Int J Solids Struct* 2005;42:3549–69.
- [30] Šmilauer V, Bittnar Z. Microstructure-based micromechanical prediction of elastic properties in hydrating cement paste. *Cem Concr Res* 2006;36: 1708–18.
- [31] Ashby MF, Evans A, Fleck NA, Gibson LJ, Hutchinson JW, Wadley HN. *Metal foams: a design guide*. Oxford, UK: Butterworth-Heinemann; 2000.
- [32] Jandejsek I, Jiroušek O, Vavřík D. Precise strain measurement in complex materials using digital volumetric correlation and time lapse micro-CT data. *Procedia Eng* 2011;10:1730–5.
- [33] Andrews E, Sanders W, Gibson LJ. Compressive and tensile behaviour of aluminum foams. *Mater Sci Eng A* 1999;A270:113–24.
- [34] Andrews EW, Gioux G, Onck P, Gibson LJ. Size effects in ductile cellular solids. Part II: Experimental results. *Int J Mech Sci* 2001;43:701–13.